# Real-Time Measurements of Actin Filament Polymerization by Total Internal Reflection Fluorescence Microscopy

Jeffrey R. Kuhn and Thomas D. Pollard
Department of Molecular, Cellular, and Developmental Biology, Yale University, New Haven, Connecticut 06520

ABSTRACT Understanding the mechanism of actin polymerization and its regulation by associated proteins requires an assay to monitor polymerization dynamics and filament topology simultaneously. The only assay meeting these criteria is total internal reflection fluorescence microscopy (Amann and Pollard, 2001; Fujiwara et al., 2002). The fluorescence signal is fourfold stronger with actin labeled on Cys-374 with Oregon green rather than rhodamine. To distinguish growth at barbed and pointed ends we used image drift correction and maximum intensity projections to reveal points where single *N*-ethylmaleimide inactivated myosins attach filaments to the glass coverslip. We estimated association rates at high actin concentrations and dissociation rates near and below the critical actin concentration. At the barbed end, the association rate constant for Mg-ATP-actin is 7.4 $\mu M^{-1}$ $s^{-1}$ and the dissociation rate constant is 0.89 $s^{-1}$. At the pointed end the association and dissociation rate constants are 0.56 $\mu M^{-1}$ $s^{-1}$ and 0.19 $s^{-1}$. When vitamin D binding protein sequesters all free monomers, ADP-actin dissociates from barbed ends at 1.4 $s^{-1}$ and from pointed ends at 0.16 $s^{-1}$ regardless of buffer nucleotide.

## INTRODUCTION

Actin polymerization contributes to many cellular processes under the control of proteins that maintain a pool of unpolymerized monomers, initiate new filaments, cap filament ends, and promote filament turnover. Understanding these mechanisms requires assays that detect not only the concentration of polymer but also the number of filaments, the direction of growth, and the presence of branches. Early studies of actin polymerization used viscometry or light scattering to measure the polymer concentration (Oosawa and Asakura, 1975), but these methods are limited because the signal depends not only on the polymer concentration, but also on the size of the filaments and the extent of cross-linking. In addition, viscometric measurements perturbed assembly by fragmenting filaments.

What was needed was a sensitive, spectroscopic assay to measure polymer concentration directly in real time. Actin labeled on Cys-374 with pyrenyl iodoacetamide filled this need (Kouyama and Mihashi, 1981), because the fluorescence of the polymer is 20 times higher than the monomer. This assay revolutionized actin research and has been the standard method for 20 years. However, this assay has limitations. First, it measures only the concentration of polymer. The direction of growth and number of filaments must be inferred, often with considerable uncertainty. Although capping proteins have been used to separate barbed from pointed end growth, these assays must assume a constant concentration of ends and thus ignore filament nucleation, annealing, and severing. Second, some proteins including myosin (Kouyama and Mihashi, 1981) and actin depolymerizing factor (ADF)/cofilin (Carlier et al., 1997) quench the fluorescence of pyrenyl-actin filaments. This is useful for binding studies, but makes it impossible to study how these proteins regulate actin polymerization. Labeling actin with 7-chloro-4-nitrobenzeno-2-oxa-1,3-diazole on Lys-373 (Detmers et al., 1981) circumvents the quenching problem, but not the uncertainty regarding the number of filaments or their direction of growth.

Fluorescence microscopy of filaments labeled with fluorescent-phalloidin (Blanchoin et al., 2000; Burlacu et al., 1992; Xu et al., 1999; Yanagida et al., 1984) reveals branches and allows measurement of filament lengths and direction of growth. Together with knowledge of the polymer concentration, this method makes it possible to calculate the number of filaments, but these insights are available only on static samples. Electron microscopy can be used to distinguish the growth at the two ends of actin filaments (Bonder and Mooseker, 1986; Pollard, 1986; Pollard and Mooseker, 1981; Woodrum et al., 1975), but this approach is also restricted to samples taken at particular time points and requires fixation in nonphysiological buffers.

An ideal assay would employ continuous observation of growing filaments, allowing documentation of the nucleation of new filaments (de novo or as branches) and growth at both ends. Fluorescence microscopy can image single actin filaments containing subunits labeled with a fluorescent dye (Cintio et al., 2001) and thus has many features of an ideal assay. To avoid interference from the sea of unlabeled actin monomers required in a polymerization experiment, the fluorescent filaments must be excited either with an evanescent wave by total internal reflection (TIR) (Amann and Pollard, 2001; Fujiwara et al., 2002) or by confocal illumination (Ichetovkin et al., 2002). Our improvements in fluorescent labeling of actin, microscope hardware, and image analysis software have made real-time microscopy of

*Submitted June 9, 2004, and accepted for publication October 27, 2004.*

Address reprint requests to Thomas D. Pollard, MCDB, KBT-548, Yale University, PO Box 208103, New Haven, CT 06520-8103. Fax: 203-432-6161; E-mail: thomas.pollard@yale.edu.



0006-3495/05/02/1387/16 $2.00

doi: 10.1529/biophysj.104.047399

actin polymerization a routine assay applicable to a wide range of actin studies (Kovar et al., 2003). We describe these improvements and characterize the elongation and the steady-state treadmilling of actin filaments.

## MATERIALS AND METHODS

### Proteins

#### *Unlabeled actin*

Actin was purified from acetone powder of rabbit skeletal muscle by one cycle of polymerization and pelleting (Spudich and Watt, 1971). We carried out all steps at 0–4°C unless specified otherwise. The pellet was resuspended in buffer G (2 mM Tris-Cl, pH 8.0, 0.2 mM ATP, 1 mM $NaN_3$, 0.1 mM $CaCl_2$, 0.5 mM dithiothreitol, DTT), sonicated for 1 min in a bath sonicator, diluted to 6 mg/ml, and dialyzed against three changes of buffer G over 2 days. After centrifugation at $10^5\times$ *g* for 2 h, the crude actin in the top 80% of the supernatant was gel filtered on Sephacryl S-300 (Amersham Biosciences, Piscataway, NJ) to separate monomers from oligomers and minor contaminants. We measured the concentration of unlabeled actin by absorbance using an extinction coefficient of $E_{290} = 26,600\,M^{-1}\,cm^{-1}$ (Houk and Ue, 1974).

#### *Labeled actin*

Crude monomeric actin was dialyzed against two changes of buffer G without DTT for 1 h each. After clarification at 500× *g* for 5 min, actin was polymerized by mixing an equal volume of cold 2× label buffer (2× = 50 mM imidazole, pH 7.5, 0.2 M KCl, 4 mM $MgCl_2$, 6 mM $NaN_3$, 0.6 mM ATP). After 5 min polymerized actin was diluted to 1 mg/ml with cold 1× label buffer. A fresh 10-mM stock solution of Oregon green 488 iodoacetamide (Molecular Probes, Eugene, OR) was prepared in *N*,*N*-dimethylformamide. A 12- to 15-fold molar excess of Oregon green was added dropwise to the actin while stirring, and the solution was stirred gently overnight. Labeled actin was clarified at 500× *g* for 5 min and centrifuged at $10^5\times$ *g* for 2 h to pellet actin filaments. The pellet was resuspended in buffer G, sonicated for 1 min, diluted to 6 mg/ml, and dialyzed for 1.5 days against two changes of buffer G and one change of buffer G6.5 (5 mM PIPES-Tris, pH 6.5, 0.2 mM ATP, 1 mM $NaN_3$, 0.1 mM $CaCl_2$, 0.5 mM DTT). After centrifugation at $10^5\times$ *g* for 2 h, the supernatant was loaded onto a 1 × 5.5-cm column of DEAE-cellulose DE52 (Whatman, Kent, UK) equilibrated with buffer G6.5 and eluted with a 200-ml gradient of 0–300 mM KCl in buffer G6.5 to separate unlabeled from labeled actin. The peak fraction and following fractions down to 30% of the peak concentration were pooled, dialyzed overnight against polymerization buffer (5 mM imidazole, pH 7.5, 0.1 M KCl, 2 mM $MgSO_4$, 0.5 mM, 0.3 mM, 0.5 mM, 1 mM $NaN_3$, and centrifuged at $10^5\times$ *g* for 2 h. The pellet was resuspended in buffer G, sonicated for 1 min, and dialyzed for 2 days against three changes of buffer G to depolymerize actin. We separated labeled actin monomers from oligomers by centrifugation at $10^5\times$ *g* for 2 h and gel filtration on a Sephacryl S-300. Fractions were stored at 4°C and remained active for up to 4 weeks. The concentration of labeled actin was measured by absorbance at 290 and 491 nm using the extinction of OG at 491 nm $E_{491} = 77,800\,M^{-1}\,cm^{-1}$ and a correction for OG absorbance at 290 nm of $A^*_{290} = A_{290} - 0.16991\,A_{491}$. The ratio of labeled actin to total actin is $[OG]/[Actin_{Total}]$.

#### *Myosin*

Rabbit skeletal muscle myosin (Kielley and Harrington, 1959) was stored at −20°C in 50% glycerol. Aliquots of ~10 μM myosin were dialyzed against 10 mM imidazole, pH 7, 0.5 M KCl, 10 mM EDTA for 2 h. After incubation with 1 mM NEM for 1 h on ice, 1 mM DTT was added for 1 h on ice. Myosin was dialyzed against 50% glycerol in 10 mM imidazole, pH 7, 0.5 M KCl, 10 mM EDTA, 1 mM DTT overnight, and stored at −20°C.

### Slide preparation

Flint glass slides of 25 × 75 × 1 mm (Erie Scientific, Portsmouth, NJ) were cleaned by a modified acid wash technique. Slides in glass vertical staining jars were sonicated for 45 min in 2% (v/v) Versaclean detergent (Fisher Scientific, Hampton, NH) in hot tap water, rinsed 10 times in hot water, and sonicated an additional 30 min. Slides were rinsed 10 times with distilled water, incubated for 3 h in 1 M KOH at 42°C, rinsed three times in double distilled (dd) water, and incubated overnight in 1 M HCl at 42°C. Jars were cooled to room temperature, rinsed five times in dd water, sonicated for 30 min in dd water, rinsed twice in 1 mM EDTA, and sonicated for 30 min in EDTA to reduce calcium contamination. Slides were rinsed twice in 70% ethanol, sonicated for 30 min, rinsed twice in absolute ethanol, sonicated for 30 min, and rinsed in absolute ethanol. Clean slides were stored in absolute ethanol in screw-top plastic jars and were used within two weeks.

### Flow cell preparation

Flow cells containing 3–5 μl of fluid were prepared each day as in Kron and Spudich (1986). Two-and-one-quarter-inch strips of parafilm were stretched to approximately three times their length and placed across the long axis of a 24 × 50-mm, No. 1 coverslip (VWR International, West Chester, PA), leaving a 2-mm gap. A clean, 25 × 75 × 1-mm flint glass slide was removed from ethanol, flamed dry, cooled, and placed perpendicular across the parafilm strips. The parafilm strips were compressed by firm hand pressure on the top of the slide to seal the sides of the chamber. The chamber was flamed again briefly and cooled to stick the protruding parafilm strips to the open coverslip surface. For an inverted microscope, chambers were used with the coverslip down, facing the objective lens, and slide up, supporting the prism. Solutions were loaded directly into the chamber via capillary action. The solution in the chamber was changed by placing 2× chamber volumes of solution at one end and then pulling it through with a piece of filter paper on the other side. To prevent fluid flow onto the top of the slide, hydrophobic ''corrals'' were drawn across the top edges of the slide, above the entrance and exit ports with room temperature VALAP (1:1:1 vaseline/lanolin/paraffin).

### Polymerization experiments

Unlabeled and labeled Ca-ATP-actin were dialyzed overnight against buffer G, centrifuged at $10^5\times$ *g* for 2 h, the supernatant concentrations measured, and mixed with buffer G to the desired labeled fraction at 2.22 times the final concentration. Ca-ATP-actin was converted to Mg-ATP-actin for each experiment by adding 1/10 part of 10× Mg exchange buffer (10 mM EDTA, 1 mM $MgCl_2$) to give two times the final actin concentration and incubating on ice for 5 min. NEM-inactivated myosin was diluted to 0.2 μM in high salt Tris-buffered saline (HS-TBS, 50 mM Tris-Cl, pH 7.6, 600 mM NaCl) containing a $10^{-4}$ dilution of 200 nm crimson fluorescent microspheres (Molecular Probes) and 5 μl were loaded into a freshly prepared flow cell. After 1 min at room temperature flow cells were washed with 10 μl 1% (w/v) bovine serum albumin (BSA) in HS-TBS followed by 10 μl 1% BSA in low-salt Tris-buffered saline (50 mM Tris-HCl, pH 7.6, 50 mM NaCl). Mg-ATP-actin (2×) was mixed 1:1 with 2× TIR buffer (100 mM KCl, 2 mM $MgCl_2$, 2 mM EGTA, 20 mM imidazole, pH 7.0, 200 mM DTT, 0.4 mM ATP, 30 mM glucose, 1% methylcellulose, 40 μg/ml catalase, 200 μg/ml glucose oxidase) and 10 μl were immediately loaded into the chamber and placed on the microscope.

### Actin filament seeds marked for polarity

Marked actin filament seeds were created as follows: 10 μM Mg-ATP-actin was mixed 1:1 with 2× TIR buffer, incubated at room temperature for 10 min to form filaments ~30 μm long, fragmented for 1 min in a bath sonicator, and incubated for 10 min. Chambers coated with NEM-myosin

and microspheres were washed once with 10 $\mu$l of 1× TIR buffer and 1 $\mu$l of seed mixture was flowed into the chamber in the reverse direction to form a gradient of seed densities on the surface. After 1 min, 10 $\mu$l of freshly prepared Mg-ATP-actin at 0.5×, 1×, or 2× the labeled fraction of seeds was mixed 1:1 with 2× TIR buffer, loaded into the flow chamber in the forward direction, and allowed to polymerize for a short time. Mg-ATP-actin was diluted to two times the desired concentration, mixed 1:1 with 2× TIR buffer, and 10 $\mu$l were loaded in the forward direction into a chamber containing preformed filaments.

## Depolymerization

Twenty-five percent labeled, 3 $\mu$M Mg-ATP-actin was mixed 1:1 with 2× ATP-TIR buffer, loaded into a flow chamber coated with NEM-myosin and microspheres, and incubated for 10 min. Chambers were washed with 25% labeled 0.18 $\mu$M Mg-ATP-actin in 1× ATP-TIR buffer, and incubated for 22 min to convert filaments to Mg-ADP-actin. Chambers were washed with 50% labeled 1.5 $\mu$M Mg-ATP-actin for 1–2 min, and washed with either 1× ATP- or ADP-TIR buffer containing 5 $\mu$M vitamin D binding protein (DBP) (Calbiochem, San Diego, CA).

## Microscope

An Olympus IX-71 microscope (Olympus America, Melville, NY) on an optical bench was modified for prism-based TIRF illumination (Fig. 1). A single-mode optical fiber (Oz Optics, Carp, Ontario, Canada) transmitted light at 488 nm from a mechanically isolated 100 mW argon-ion laser (Midwest Laser Products, Frankfort, IL). The 3-mm beam was passed through a 5× beam expander and an active phase scrambler (a transparent plastic petri dish spinning at >1000 rpm) to remove interference patterns due to stray light and produce even excitation illumination. Two dielectric mirrors steered the beam to the microscope stage at a 13° angle from the horizontal, where it was focused with an $f = 100$ mm convex lens onto a right-angle prism attached to a flow cell by a thin layer of glycerol. The exit beam was absorbed by a beam block. Optics and optomechanics were from Thorlabs (Newton, NJ). Uniblitz shutters (Vincent Associates, Rochester, NY) controlled the illumination from the laser and arc lamp. A motorized filter turret (Olympus) switched filter cubes, and a Mac 5000 stepper motor controlled focus (Ludl Electronic Products, Hawthorne, NY). Images were captured with an Orca-ER charge-coupled device camera (Model C4742-95-12ER, Hamamatsu, Bridgewater, NJ). A custom-designed image acquisition plug-in for the public domain image analysis program, ImageJ (National Institutes of Health, http://rsb.info.nih.gov/ij/), controlled the microscope filter wheel, shutters, focus, and camera.

## Autofocus

Imaging a field of subresolution, crimson fluorescent microspheres (Molecular Probes) on the chamber surface was used to select the best focal plane for TIR imaging. Before each time lapse TIR exposure through a fluorescein filter cube (Chroma Technology, Rockingham, VT), a rhodamine filter cube (Chroma) was rotated into place, the epifluorescence shutter was opened and eight images, spaced at $Z$ axis increments of 1 $\mu$m, were taken of the field of beads. Each image $I_{xy}(z)$ was convolved with a derivative of a Gaussian filter. The resulting $x$- and $y$-derivative images were summed, squared, and added together to form a single focus value at each $z$-position,

$$f(z) = \left(\sum_{x=1}^{W}\sum_{y=1}^{H}\frac{dG_x}{dx}\otimes I_{xy}(z)\right)^2 + \left(\sum_{x=1}^{W}\sum_{y=1}^{H}\frac{dG_y}{dy}\otimes I_{xy}(z)\right)^2, \quad (1)$$

where

$$G_x = \frac{1}{\sqrt{2\pi\sigma^2}}\exp\left(\frac{-x^2}{2\sigma^2}\right). \quad (2)$$

$G_y$ was similarly defined in the $y$-direction, and $W$ and $H$ were the image width and height, respectively. A Gaussian width of $\sigma = 2$ was used. The $z$-value, which maximized $f(z)$, was estimated using parabolic interpolation of the sampled maximum focus value $f_k$, and its two nearest neighbors $f_{k-1}$ and $f_{k+1}$.

$$z_{max} = z_0 + k\Delta z + \frac{1}{2}\frac{f_{k-1} - f_{k+1}}{2f_{k-1} - 2f_k + f_{k+1}}\Delta z. \quad (3)$$

The best-focus position was further refined by using the estimated $z$-value as the center position of eight new epifluorescent images, spaced $\Delta z = 0.25\mu$m apart, and the focus function and best-focus position are recalculated. Because this autofocusing process is very insensitive to noise, short exposure times could be used, and the entire focus process was completed in <5 s.

## Drift correction

The drift correction algorithm was written in Java as a plug-in for ImageJ. Drift was typically corrected in two phases. In the first phase, a single bright fluorescent speckle was roughly tracked by hand through every frame. The tracking was refined to the center of the speckle at each frame as follows. The image was smoothed by convolution with a Gaussian kernel of $\sigma = 1$–$2$ pixels in radius to reduce image noise. Local pixels within a certain radius (typically 5–20) of the initial track point were searched for the maximum intensity. The position of the peak intensity was further refined to subpixel accuracy in both $x$- and $y$-directions by parabolic interpolation between the peak pixel $I_{m,n}$ and its two neighbors in either $x$ or $y$ as follows. Given an $x$-position of $m$, the discrete first and second derivative of the intensity in the $x$-direction are $(dI/dx) = (I_{m+1,n} - I_{m-1,n})/2$ and $(d^2I/dx^2) = 2I_{m,n} - I_{m+1,n} - I_{m-1,n}$, respectively. The new $x$-position of the peak of the parabola is estimated from $m_{peak} = m + (dI/dx)/(d^2I/dx^2)$. The $y$-position of the peak $n_{peak}$ is estimated in the same way. Once the speckle centers were refined in each frame, the position of the speckle in the first frame was subtracted to obtain the drift over time. Each image was shifted in the opposite direction, using bilinear interpolation to estimate the intensity of fractional pixel positions.

In the second correction pass, the positions of several particles were roughly marked in the first frame. The centers of each particle were then found in each frame using the radial search and parabolic refinement above. The average change in position of all particles was then calculated as the average drift of the entire image sequence. Each image was again shifted in the opposite direction using bilinear interpolation of the old image to obtain the new pixel intensities.

## Data analysis

We wrote filament snapping and length measurement algorithms in Java as plug-ins for ImageJ. For each experiment, we performed drift correction on the entire image sequence and created an MIP of the entire sequence that was added to the end of the image sequence stack. Each pixel in the MIP represented the maximum intensity of that pixel over all time points. We selected single filaments for analysis, one at a time. A straight line drawn across the filament's myosin restriction point in the MIP was recorded as the cutting line. For each time point, we traced the filament with a rough, freehand polygon, taking care to accurately mark the filament endpoints. The filament trace was refined through several steps. The curve was first smoothed by downsampling a Cartesian Fourier descriptors representation of the polygon (Jähne, 2002) as follows. The freehand polygon was converted to a ''closed'' curve by doubling each point such that the curve

was traced first in the forward direction, then the opposite direction. Each original endpoint was further replicated in place twice to ''fix'' its position. The $x$- and $y$-positions of each point $\mathbf{P}_n = (x_n, y_n)$ in the closed curve of $N$ points were combined into a complex number representation $z_n = x_n + i\,y_n$. The sequence of $z$-values was converted into a Fourier series representation by calculating $P = N$ Fourier coefficients using a discrete Fourier transform

$$Z(s) = \frac{1}{N}\sum_{n=0}^{N-1} z_n \exp\left(-i\frac{2\pi\, s\, n}{N}\right), \tag{4}$$

where each of the coefficient $Z(s)$ represents successive approximations of the curve. The original curve could be reconstructed from these Fourier coefficients by means of an inverse Fourier transform

$$z_n = \sum_{s=0}^{P} Z(s)\exp\left(i\frac{2\,\pi\, n\, s}{P}\right). \tag{5}$$

The original curve was smoothed by reconstruction from fewer Fourier coefficients. To reduce the number of points to half, only the first $P/2$ coefficients are used to reconstruct the curve. The polygon curve was then converted to an ''open'' curve by removing the second half of its points, effectively tracing the path only in the forward direction.

Once we obtained a smooth, downsampled version of the rough filament trace, the trace was refined to the centerline of the filament as follows. The entire image was smoothed by convolution with a Gaussian convolution kernel of $\sigma = 1$–$2$ pixels in radius. For each point along the line $\mathbf{P}_n = (x_n, y_n)$, the estimated direction tangent to the filament was obtained by vector subtraction of the next and previous points $\mathbf{u}_n = \mathbf{P}_{n+1} - \mathbf{P}_{n-1}$. The direction perpendicular to the filament at that point was then $\mathbf{v}_n = (-u_{y,n}, u_{x,n})$. The smoothed image was sampled at 1-pixel increments along this perpendicular direction for a radius of 5 pixels in either direction. The intensities of fractional pixel positions were estimated by bilinear interpolation to obtain the intensity profile perpendicular to the line. This profile was searched for a local maximum intensity that was closest to the original point. The maximum intensity along this perpendicular direction was further refined by one-dimensional parabolic interpolation with its two nearest neighbors in the profile. The position of this maximum intensity was taken as the filament center, and the current point was moved to this point. This refinement process could be iterated a second time to further define the center of the filament. When filament density was high, the refinement process would occasionally cause the filament trace to ''jump'' to a nearby filament. In these instances, the filament could be traced again, the search radius could be decreased to 3 pixels in either direction, or the refinement process could be limited to one iteration.

The refined filament trace was used to measure the length of the entire filament and the lengths on either side of the cutting line defined earlier. The polygon representing the filament trace was followed from start to finish. The length of each segment of the polygon was calculated, and each segment was tested for intersection with the cutting line. Each time an intersection was found, the segment was cut at that point, the current length from either the filament start or the last intersection point was recorded, and the process continued from the intersection point until the other end of the filament was reached. Kymographs were produced by segmenting the refined filament trace polygon into 1-pixel-long intervals. The intensity at each vertex was estimated with bilinear interpolation of the nearest four pixels. The entire process of image smoothing, refinement of the hand trace, and length measurement took roughly 1 s. For each filament, the measurement process was repeated at each time point to obtain the total filament length over time and lengths between both ends and the cutting line.

Instantaneous rates were calculated with a windowed derivative filter. For each filament end, the measured lengths $L$ at each frame $t$ were combined into a list, $L_t$. Any missing frames were filled by linear interpolation of the two closest measured lengths. The beginning of the list was extended backward in time by linear extrapolation of the first two length measurements. The end of the list was extended forward in a similar fashion. The entire list was convolved with a derivative of a Gaussian filter,

$$G_t = \frac{-t}{\sigma^2}\frac{1}{\sqrt{2\pi\sigma^2}}\exp\left(\frac{-t^2}{2\sigma^2}\right), \tag{6}$$

with a half-width, $\sigma$, of two to three frames and divided by the average time between frames for the experiment. This simultaneously smoothed the data and calculated the change in length. Instantaneous rates for extrapolated frames were thrown out.

## RESULTS

### Improved hardware for imaging actin polymerization

We modified the prism-based total internal reflection light source on an inverted epifluorescence microscope (Amann and Pollard, 2001) (Fig. 1). An inexpensive (BK7) right-angle glass prism served as well as a quartz Pellin Broca prism. An active phase scrambler consisting of clear plastic plate spinning at >1000 rpm after the beam expander scrambled the laser polarization and smoothed out intensity variations in the total internal reflection fluorescence (TIRF) illumination due to interference patterns and stray light. An automated filter cube turret and shutters for both the laser and arc lamp light sources allowed rapid switching between TIRF and epifluorescence illumination. A stepper motor attached to the microscope fine focus wheel permitted automated focusing of the TIRF image.

### Actin labeled with Oregon green 488 on Cys-374 incorporates into growing filaments

The work described here was done with actin labeled on Cys-374 with the stable fluorescein derivative, Oregon green 488 iodoacetamide (OG-actin). OG-actin copolymerized

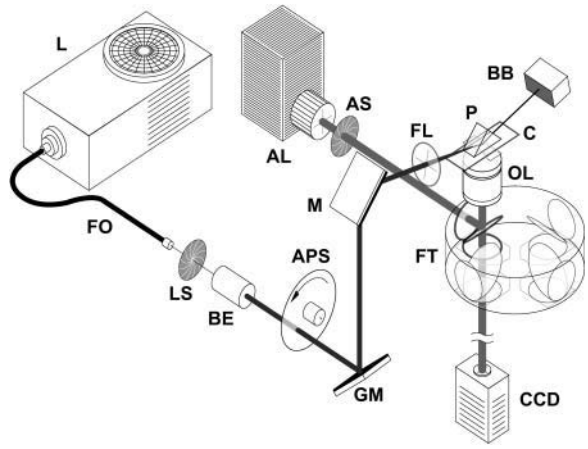


FIGURE 1 Diagram of the inverted microscope modified for total internal reflection fluorescence illumination. L, laser; FO, fiber optic; LS, laser shutter; BE, 5× beam expander; APS, active phase scrambler; GM, Gimbal-mounted mirror; M, mirror; FL, 100-mM plano-convex focusing lens; P, 10-mm right-angle prism; C, flow chamber; BB, beam block; AL, mercury arc lamp; AS, arc-lamp shutter; FT, automated filter cube turret; OL, 1.4-N.A., 60× objective lens; CCD, cooled charge-coupled device camera.

with unlabeled actin. The emission intensity of polymerized OG-actin was 4.5 times that of actin filaments labeled on Cys-374 with rhodamine maleimide, the conjugate used by Amann and Pollard (2001) and others (Fujiwara et al., 2002).

TIRF microscopy allowed imaging of individual actin filaments polymerizing from mixtures of OG-actin monomers and unlabeled actin monomers (Fig. 2 *A*). We observed the growth of filaments in the presence of 0.5–5 $\mu$M total Mg-ATP-actin including 10–50% OG-actin. The contrast was excellent even with micromolar concentrations of unpolymerized fluorescent actin in solution. On the other hand, the high background fluorescence of unpolymerized molecules prevented imaging of polymerizing OG-actin filaments by epifluorescence microscopy.

We followed the growth of individual filaments by recording time-lapse images every 8–30 s, the interval depending on actin monomer concentration. Growth could be followed for more than an hour with 0.5 $\mu$M actin monomers, but with 5 $\mu$M actin monomers the density of labeled filaments on the surface of the slide obscured individual filaments by 7 min.

## Myosin attachment points distinguished growth at barbed and pointed ends

A fiducial mark is required on each filament to distinguish the growth at the two ends. We used single *N*-ethylmaleimide (NEM)-inactivated myosin II molecules to attach filaments to the chamber surface (Amann and Pollard, 2001), but locating and using these tethers as external reference marks required correction of stage drift. We developed software to track several stationary fluorescent particles in the field of view (Fig. 3 *A*) with subpixel accuracy. We took the average motion of these particles as the total drift over the course of an experiment and used this measurement to shift each image in the opposite direction and stabilize the entire movie (Fig. 3 *C*). We combined each TIRF microscopy sequence into a single image with a maximum intensity projection (Fig. 3, *B* and *C*), where each pixel in the projection image corresponded to the maximum intensity projection (MIP) at that location over all time points. The MIP image exposed the history of each filament and revealed constriction points where the Brownian motion of a swiveling filament was negligible (Fig. 3 *C*, *arrows*). We verified that these restriction points were fixed at a point on the filaments by changing the mol fraction of OG-actin midway through a polymerization experiment. Such sharp steps in fluorescence intensity rarely moved with respect to the constriction point of the filament, even over several hours (Fig. 3 *C*). We used constriction points to separate the two ends during length measurements. We assumed that barbed ends grow faster than pointed ends.

We developed software to measure the length of each filament end through several frames. The software converted a rough hand trace of a filament into a refined measurement by snapping each point along the trace to the filament center and endpoints. The refined trace was cut into two segments at the external fiducial point and the total length and lengths of each segment were computed. We repeated this process over several frames to obtain growth curves for both ends of each filament.

We eliminated from analysis filaments that moved from their constriction points, due to detachment from myosin or incorrect assignment of an attachment point. Sliding of nongrowing filaments would appear as coordinated movements of the two ends relative to the point chosen as the constriction point. Detection of sliding is more difficult for growing filaments. Filament sliding would appear as coordinated movements of the two ends superimposed on their linear growth curves (Fig. 4, *A* and *C*), but would not affect the total filament length. We detected nonlinearities in length traces by subtracting the length estimated by linear regression from the measured length. We used such residual plots to search for coordinated nonlinear movement of the barbed and pointed ends of a filament, and linear growth of the entire filament. Plots of length residuals at the two ends of filaments as a function of time revealed two classes of filaments.

Some filaments remained fixed at the constriction point. These filaments grew steadily at both ends over time (Fig. 4, *A* and *C*). Elongation was much faster at barbed ends and plots of length as a function of time barely deviated from linearity (Fig. 4 *A*). Elongation was slow at pointed ends and the measurements were noisy owing to the small changes in length and measurement error. The residuals from barbed end length measurements and the negative residuals from pointed end length measurements were uncorrelated (Fig. 4 *E*); addition or subtraction of the residuals gave the same result, indicating that the errors were random. This test validated the constriction points of such filaments as accurate fiducial marks.

Other filaments slid along their lengths relative to their constriction points. Plots of length as a function of time deviated from linearity at both ends (Fig. 4, *B* and *D*), with coordinated fluctuations in the distances between the constriction point to the two ends (Fig. 4 *F*). The residuals from barbed end length measurements and the negative residuals from pointed end length measurements were correlated (Fig. 4 *F*). If the difference between the two end residual measurements was $>130\%$ of the measurement error for the total filament length (equivalent to the sum of the two end residuals), the filament was defined as not fixed at the constriction point and rejected as unsuitable for measuring growth at the two ends.

## Autofocusing

We used subresolution crimson fluorescent beads as autofocusing targets during long-term TIRF recordings of actin filaments. We coated flow cells with 5–20 beads per

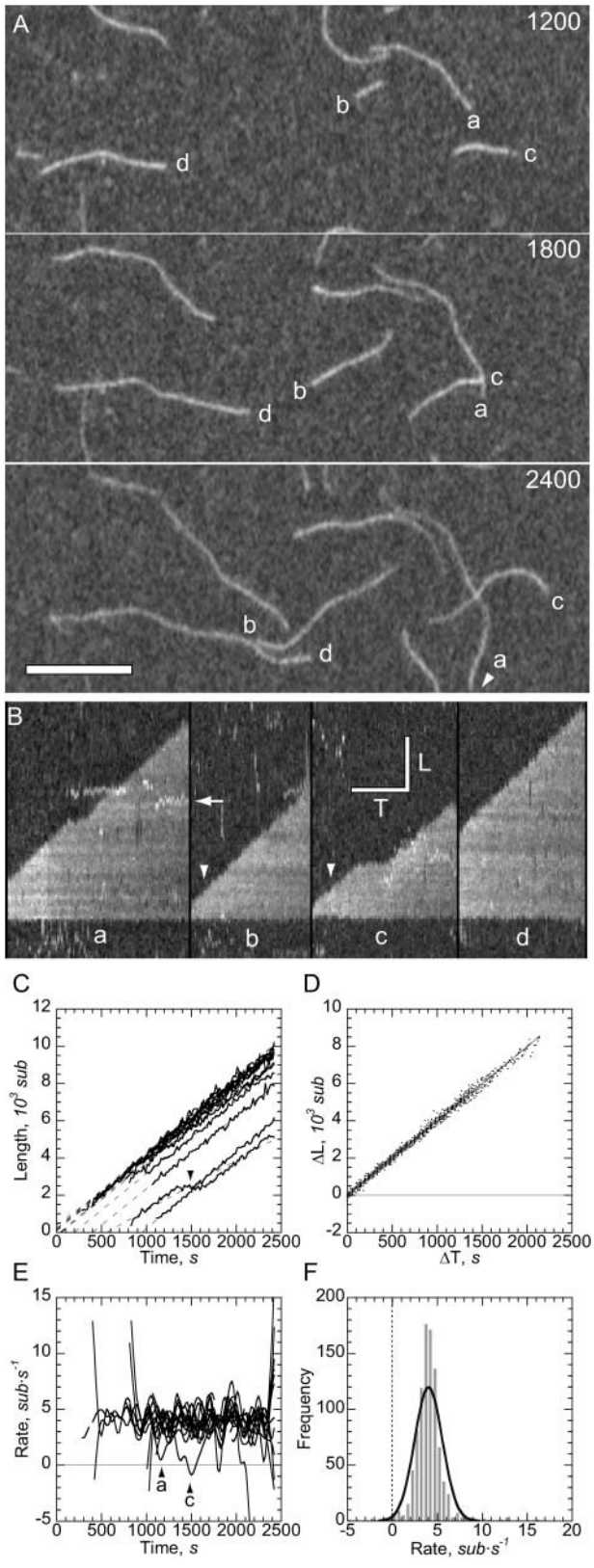


FIGURE 2 Imaging the time course of the polymerization of Mg-ATP-actin. Conditions: 1.5 $\mu$M (30% Oregon green 488 labeled) Mg-ATP-actin, 10 mM imidazole, pH 7.0, 50 mM KCl, 1 mM $MgCl_2$, 1 mM EGTA, 100 mM DTT, 0.2 mM ATP, 50 $\mu$M $CaCl_2$, 15 mM glucose, 20 $\mu$g/ml catalase, 100 $\mu$g/ml glucose oxidase, 0.5% methylcellulose at 25°C. (*A*) Labeled actin was mixed with polymerization buffer, placed in a flow chamber previously coated with 0.2 $\mu$M NEM-inactivated myosin and blocked with 1% BSA. Growing barbed ends of four filaments are marked as *a–d*. Numbers are seconds after adding polymerization buffer. Scale bar is 20 $\mu$m. (*B*) Linear kymographs of the growing filaments marked in panel *A*. Intensities were sampled at 1-pixel increments along each filament center (*vertical axis*) for several consecutive frames (*horizontal axis*) starting from the pointed end (*bottom*). Barbed-end growth occasionally stalled (*a* and *c*). Arrowheads indicate low speckle contrast. Length scale bar (*L*) is 10 $\mu$m and timescale bar (*T*) is 1000 s. (*C*) Lengths of 13 filaments as a function of time (*solid lines*) expressed in subunits, calculated using 370 subunits/$\mu$m (Huxley and Brown, 1967). Dashed lines are linear fits of each filament growth trace. Arrowhead indicates filament pause. The average slope was 3.9 $\pm$ 0.4 $s^{-1}$. (*D*) Change in length of 13 filaments as a function of time. Individual growth traces were combined by subtracting each filament's starting length (based on the linear fit) from total length and start time from total time for each data point. Length measurements for stalled barbed ends were disregarded. A single rate of 3.974 $\pm$ 0.010 sub·$s^{-1}$ (*solid line*) was assigned to the entire sequence ($N = 925$) by linear regression. (*E*) Instantaneous growth rates of filament shown in panel *C*. A Gaussian smoothing window was applied to each filament's length measurement and the change in smoothed length per change in time is shown. Rates near zero indicate filament growth stalls. Markings (*a* and *c*) correspond to stalling filaments shown in panel *B*. (*F*) Distribution of smoothed instantaneous growth rates for all length measurements with stalled sections removed. Rates were binned into 0.5 $s^{-1}$ increments and plotted as a histogram of observation frequency for each binned rate (*shaded bars*). A Gaussian distribution (*solid line*) corresponding to the average measured instantaneous rate of 4.0 and $\pm$ SD of 1.5 $s^{-1}$ ($N = 925$) is shown for comparison.

field concurrently with NEM-myosin-II. Before acquiring each TIRF image, the microscope took a Z-series of epifluorescent images of the beads at a longer wave length, using short exposures and low light levels to avoid bleaching of Oregon green. We measured focus using a standard sharpness function. Because a focused image is sharper than an out-of-focus image, the total image derivative $(dI/dx)^2 + (dI/dy)^2$ summed over all pixels is maximal at the correct focal plane. This two-pass autofocusing step proved robust even for extremely noisy images, took $<5$ s, and kept filaments in focus more than several hours. This method avoids bleaching that would occur if the microscope were focused on the filaments before acquiring each image.

## Speckles

Fluorescent speckles are an alternative to single molecule tethers as fiducial marks. With the mol fractions of labeled actin employed here, ''speckles'' of nonuniform labeling along filaments were rarely discernable in single images (Fig. 2 *A*) but were obvious in straightened intensity kymographs of filaments (Fig. 2 *B*) as persistent dark patches. Because speckle contrast was often low (Fig. 2 *B*, *arrowheads*) and filament overlap could also produce speckles (Fig. 2 *B*, *arrow*), myosin tethers were used as fiducial marks for this study. Nevertheless, these dark speckles rarely moved relative to the myosin tether points (not shown),

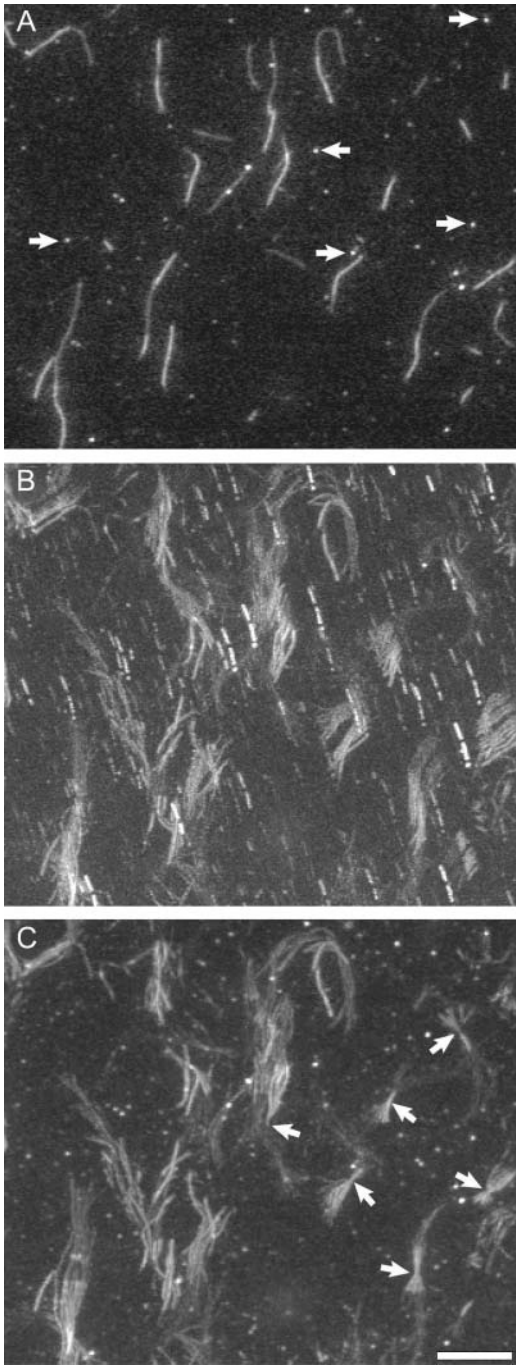


FIGURE 3 Drift correction reveals NEM-myosin attachment points useful as fiducial marks to separate barbed from pointed ends. Conditions: same buffer as Fig. 2. Actin filaments with segments of different fluorescence intensity were created by loading the chamber sequentially with polymerizing buffer containing 5 $\mu$M 25% labeled actin, followed by 5 $\mu$M 50% labeled actin, followed by 0.175 $\mu$M 25% labeled actin. (*A*) Image of a field at 10 s after addition of the final actin concentration, showing sequentially labeled filaments. Dim segments of the filaments are pointed ends, bright segments are barbed ends. Annealing created filaments with multiple bright segments. Bright spots of fluorescent material from the actin sample (*arrows*) remained stationary relative to each other. (*B*) The intensity of each image in the sequence (25 frames; 2 h total) was normalized and the sequence was combined into a single image with a maximum intensity projection. In this life-history image, both filaments and the bright spots moved as the stage drifted. (*C*) Maximum intensity projection. Several bright spots were tracked with subpixel accuracy and the average positions were used to estimate the drift at each time point. Each image was shifted in the reverse direction to compensate for the drift. Several filaments exhibited constriction points (*arrows*) around which the filaments rotated over time. Labeled fiducial marks (the boundaries of segments differing in intensity) did not move with respect to these constriction points over 2 h. Scale bar is 20 $\mu$m.

verifying that our constriction point method of end separation was also valid for a single mol fraction of label.

## Steady growth interrupted by pauses

The total length of most filaments increased at a constant rate for many minutes (Fig. 2 *C*) indicating that the actin monomer pool was not depleted. Pauses interrupted periods of steady growth at all concentrations of monomers (Fig. 2, *C* and *E*, *arrowheads*). We removed obvious pauses of three or more frames (24–90 s depending on the frame rate) from rate analysis measurements.

We analyzed the elongation data in experiments such as Fig. 2 in three ways: 1), individual filament slopes; 2), pooled filaments slope; and 3), distribution of instantaneous growth rates. For 1.5 $\mu$M (30% labeled) Mg-ATP-actin, individual filaments (method 1; Fig. 2 *C*) elongated at an average of $3.9 \pm 0.4$ subunits $\times$ $s^{-1}$ ($N = 13$ filaments). Using the same data, all filaments in the field were combined as the change of length of each filament with time (method 2; Fig. 2 *D*). All of the points fell along the same line with a slope of $3.914 \pm 0.010$ subunits$\cdot s^{-1}$ ($N = 925$ data points), indicating that growth was uniform throughout the field. Alternatively, we smoothed each filament length trace with a Gaussian window and calculated the change in length over each four-frame interval (Fig. 2 *E*) to obtain a distribution of rates (method 3). The instantaneous rates had a Gaussian distribution (Fig. 2 *F*) with an average change in length of $4.0 \pm 1.5$ subunits$\cdot s^{-1}$ ($N = 925$ data points). We consider the merits of each approach below.

## OG-actin monomers incorporate into filaments but do not contribute to elongation rates

Like actin labeled with rhodamine on Cys-374 (Amann and Pollard, 2001), actin labeled on Cys-374 with Oregon green 488 depended on unlabeled actin for polymerization. At both 1 $\mu$M and 2.5 $\mu$M total Mg-ATP-actin, the elongation rates at the barbed end were inversely proportional to the fraction of labeled actin (Fig. 5 *C*). Extrapolation of this linear trend line to 0% label gave polymerization rates expected for native, unlabeled actin (Pollard, 1986). Linear extrapolation of this data gave no barbed end elongation at 90% label, similar to rhodamine-Cys-374-actin (Amann and Pollard, 2001). Noise obscured any dependence of pointed end

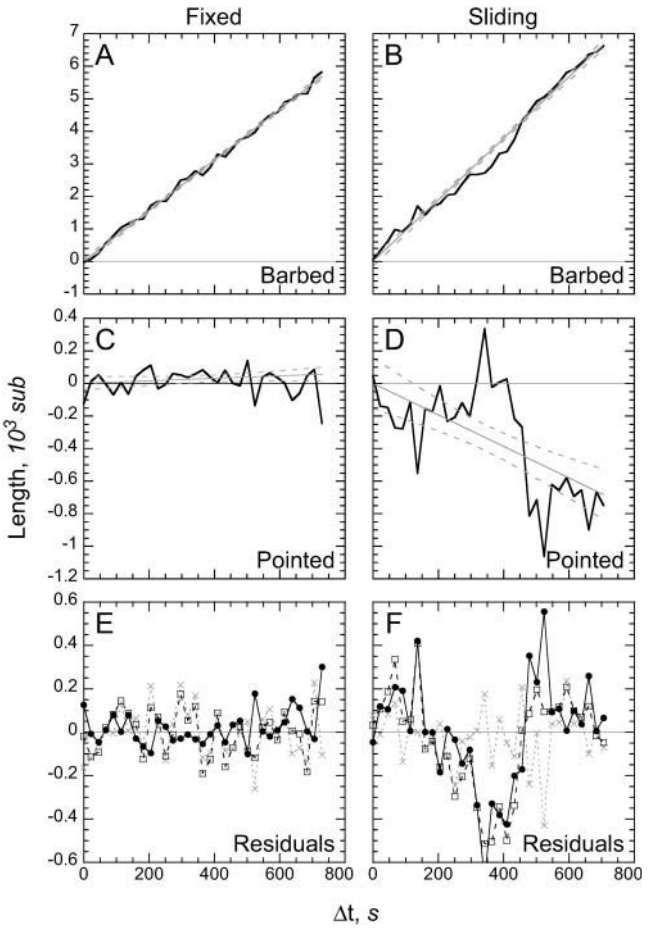


FIGURE 4 Residual analysis of length as a function of time data is used to separate affixed and sliding filaments. Conditions: 2 $\mu$M, 30% labeled Mg-ATP-actin was polymerized and the resulting sequence was corrected for drift and combined with a maximum intensity projection. Barbed and pointed ends were separated during length measurements by transection with a line drawn across a constriction site. Change in length as a function of change in time for (*A* and *B*) barbed ends and (*C* and *D*) pointed ends. Growth rates were obtained by robust linear regression. (*E* and *F*) Residuals of the barbed end (□, *dashed line*, measured length minus fitted length), negative residuals of the pointed end (●, *solid line*, fitted minus measured length), and residuals of total filament length (×, *dotted line*, measured minus fitted total length). (*A*, *C*, and *E*) An example of a filament fixed at its constriction point with no correlation between barbed and pointed end residuals. (*B*, *D*, and *F*) An example of a filament sliding over its constriction point with correlated barbed end and pointed end residuals.

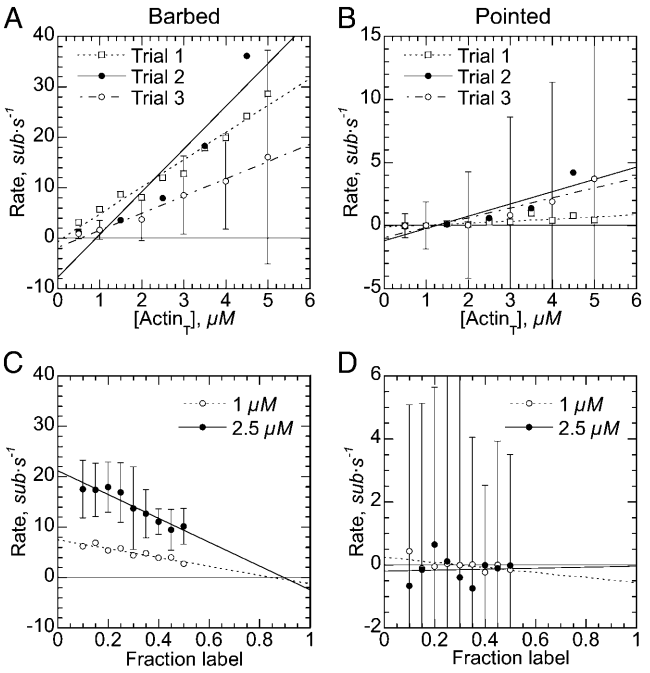


FIGURE 5 Dependence of polymerization rates on actin concentration and fraction of labeling. Conditions: Mg-ATP-actin in same buffer as Fig. 2. (*A* and *B*) Dependence of elongation rates at (*A*) the barbed end and (*B*) pointed end on the concentration of 30% labeled actin ($f_{OG} = 0.3$). Eight to 15 filaments fixed at their constriction points were selected at each concentration. Barbed and pointed end lengths of each filament were measured over 10–60 frames, and rates were obtained by averaging smoothed instantaneous growth rates for every measurement. Three trials using two different actin preparations are shown. Rate constants (□, *solid line*) for trial 1 of $k_+^B = 5.4 \pm 0.4\,\mu M^{-1}\,s^{-1}$, $k_-^B = 0.8 \pm 1.2\,s^{-1}$, $k_+^P = 0.17 \pm 0.05\,\mu M^{-1}s^{-1}$, $k_-^P = 0.14 \pm 0.16\,s^{-1}$; (●, *dashed line*) for trial 2 of $k_+^B = 8.5 \pm 1.8\,\mu M^{-1}\,s^{-1}$, $k_-^B = 7 \pm 5\,s^{-1}$, $k_+^P = 1.0 \pm 0.3\,\mu M^{-1}\,s^{-1}$, $k_-^P = 1.2 \pm 0.8\,s^{-1}$; and (○, *dashed-dotted line*) for trial 3 of $k_+^B = 3.4 \pm 0.2\,\mu M^{-1}\,s^{-1}$, $k_-^B = 1.8 \pm 0.7\,s^{-1}$, $k_+^P = 0.79 \pm 0.16\,\mu M^{-1}\,s^{-1}$, $k_-^P = 1.0 \pm 0.5\,s^{-1}$ were obtained by linear regression. Standard distributions of instantaneous rate measurements are shown for trial 3. Similar distributions were seen for trial 1 and trial 2. Trials 2 and 3 were from the same preparation on separate days. (*C* and *D*) Dependence of elongation rates at the (*C*) barbed end and (*D*) pointed end on the mol fraction of labeled actin. Mg-ATP-actin with 10–50% of the molecules labeled was polymerized at (○, *dashed line*) 1 $\mu$M and (●, *solid line*) 2.5 $\mu$M total actin and average smoothed instantaneous growth rates were fitted with linear regression.

elongation rates on the fraction of labeled actin (Fig. 5 *D*). We were unable to obtain 100% labeled OG-actin to demonstrate directly its incapacity of polymerize.

## Barbed end elongation above the critical concentration

To obtain the association and dissociation rate constants for Mg-ATP-actin polymerization, we measured barbed and pointed end growth of 30% labeled Mg-ATP-actin over a 10-fold range of actin concentrations (0.5–5 $\mu$M; Fig. 5 *A*). Assuming linear growth (see Fig. 2, *B* and *C*), we estimated the measurement error from the residuals of plots of filament lengths versus time. The average errors for single measurements of length were $150 \pm 60$ subunits for barbed ends and $140 \pm 70$ subunits for pointed ends ($N = 318$ filaments), about twice the microscope's resolution limit of 81 subunits (220 nm). These measurement errors were small compared to the length changes at barbed ends (Fig. 5 *A*) but large relative to the length changes at pointed ends (Fig. 5 *B*).

In each of three experiments, plots of elongation rates versus total actin concentration (labeled + unlabeled) were linear but the slopes differed between experiments. Fitting

the average instantaneous growth rate (method 3; Fig. 2 *F*) at each concentration to a line gave superior correlation coefficients than either fitting to individual filaments (method 1; Fig. 2 *C*) or pooled filaments (method 2; Fig. 2 *D*) at each concentration. For 30% labeled actin, the barbed end association rate constants for trials 1–3 were $k_+^{b,30\%} = 5.4 \pm 0.4$, $8.5 \pm 1.8$, and $3.4 \pm 0.2\ \mu M^{-1}\ s^{-1}$, respectively, and the barbed end dissociation rate constants for trials 1–3 were $k_-^{b,30\%} = 0.8 \pm 1.2$, $8 \pm 5$, and $1.8 \pm 0.8\ s^{-1}$. Knowing that labeled actin did not contribute to elongation rates, we combined the rates for all measured actin concentrations and labeled fractions (Fig. 5, *A–D*) into a single plot of rate versus concentration of unlabeled Mg-ATP-actin. For barbed ends (Fig. 8 *C*, *circles*), every filament showed the same dependence of rate on the concentration of unlabeled actin, regardless of the concentration of OG-actin in the experiment. From this combined plot, the barbed end association rate constant for unlabeled actin was $k_+^b = 7.5 \pm 0.7\ \mu M^{-1}\ s^{-1}$ and the dissociation rate constant was $k_-^b = 1.0 \pm 1.2\ s^{-1}$.

Pointed ends grew slowly and measurement errors were large compared to the average change in length. Individual pointed end growth rates varied significantly more than barbed end growth rates due at least in part to this measurement error. Nevertheless, pointed end growth rates increased with actin concentration (Fig. 5 *B*). A linear fit to this data gave pointed end rate constants for trials 1–3 of $k_+^{p,30\%} = 0.17 \pm 0.05$, $1.0 \pm 0.3$, and $0.79 \pm 0.16\ \mu M^{-1}\ s^{-1}$ and $k_-^{p,30\%} = 0.14 \pm 0.16$, $1.2 \pm 0.8$, and $1.0 \pm 0.5\ s^{-1}$, respectively. A combined plot of rate as a function of unlabeled actin (Fig. 8 *D*, *circles*) gave rate constants of $k_+^p = 0.66 \pm 0.14\ \mu M^{-1}\ s^{-1}$ and $k_-^p = 0.7 \pm 0.2\ s^{-1}$.

## Subunit dissociation from barbed and pointed ends in the absence of free Mg-ATP-actin monomers

To measure subunit dissociation in the absence of association, we used 5 $\mu$M vitamin D binding protein (DBP) ($K_d \sim 1$ nM for ADP-actin monomers; McLeod et al., 1989) to sequester monomers as they dissociated from filament ends. Actin filaments assembled on the slide from 25% labeled Mg-ATP-actin were aged under treadmilling conditions (0.18 $\mu$M Mg-ATP-actin monomers) for 22 min (5× half-times for phosphate release) to convert them predominantly to ADP-actin. We marked barbed ends briefly with 50% labeled Mg-ATP-actin, before washing out actin monomers and adding DBP in buffer containing either ATP or ADP. Although different labeled fractions at barbed ends might complicate measurements, less than one-third of the measured filaments were marked, and the brightly labeled segments depolymerized quickly. Because depolymerization of some filaments slowed or stopped after ~20 min, we measured depolymerization rates during the first 1000 s.

Marked barbed ends of ADP filaments shortened at rates of $2\ s^{-1}$ in ATP buffer, whereas pointed ends shortened at $0.2\ s^{-1}$. Based on this 10-fold difference in depolymerization rates, we designated the rapidly depolymerizing ends of unmarked filaments as barbed ends and combined marked and unmarked filaments for further analysis. The distribution of smoothed instantaneous rates at barbed ends was Gaussian with a mean dissociation rate of $1.23 \pm 2.88\ s^{-1}$ (mean ± SD; Fig. 6 *A*). The distribution was skewed slightly toward a dissociation rate of zero, consistent with long pauses in depolymerization observed for several filaments. All pointed end depolymerization rates clustered in one peak with a mean of $0.06 \pm 1.89\ s^{-1}$ (Fig. 6 *B*). In buffer containing ADP Mg-ADP-actin filaments also shortened faster at their barbed ends ($1.52 \pm 2.86\ s^{-1}$; Fig. 6 *C*) than at their pointed ends ($0.26 \pm 2.20\ s^{-1}$; Fig. 6 *D*).

## Subunits treadmill through actin filaments under nonequilibrium conditions

Theoretical studies of actin polymerization predicted (Wegner, 1976) and measurements of rate constants verified (Pollard, 1986; Pollard and Mooseker, 1981) that once actin filaments reach a steady state, the concentration of Mg-ATP-actin monomers is slightly above the critical concentration at the barbed end and well below the critical concentration at the pointed end. Under these conditions a population of filaments has net elongation of barbed ends matched by net shortening of pointed ends. Although total polymer concentration remains constant, subunits treadmill through filaments from the barbed to the pointed end. Fujiwara et al. (2002) were the first to observe single filaments growing at their barbed ends and shrinking at their pointed ends by TIRF microscopy.

We extended this work by observing the behavior of filaments over a range of Mg-ATP-actin monomer concentrations from 0.025 to 0.2 $\mu$M. Under these conditions the critical concentration at the barbed end is 0.1 $\mu$M and the critical concentration at the pointed end is 0.8 $\mu$M. To distinguish the two ends of these filaments, we pulse-labeled long filaments with 50% labeled actin at the pointed end and 35% labeled actin at the barbed end, then exchanged the solution in the chamber with a low concentration of 25% labeled actin monomers to observe filaments under treadmilling conditions (Fig. 7). The ends of the filaments changed length very slowly. For example, in 150 nM Mg-ATP-actin, pointed ends take ~40 min to shorten 1 $\mu$m. Thus, accurate measurements of treadmilling rates by TIRF microscopy required autofocusing to collect images for more than an hour.

The behavior of the two ends depended on the actin monomer concentration. With Mg-ATP-actin monomer concentrations ≤100 nM (75 nM unlabeled actin), both ends shortened. At slightly higher concentrations, barbed ends elongated and pointed ends shortened. Fig. 7 *A* shows time series of four filaments treadmilling in 150 nM total monomeric actin. At this concentration, barbed ends

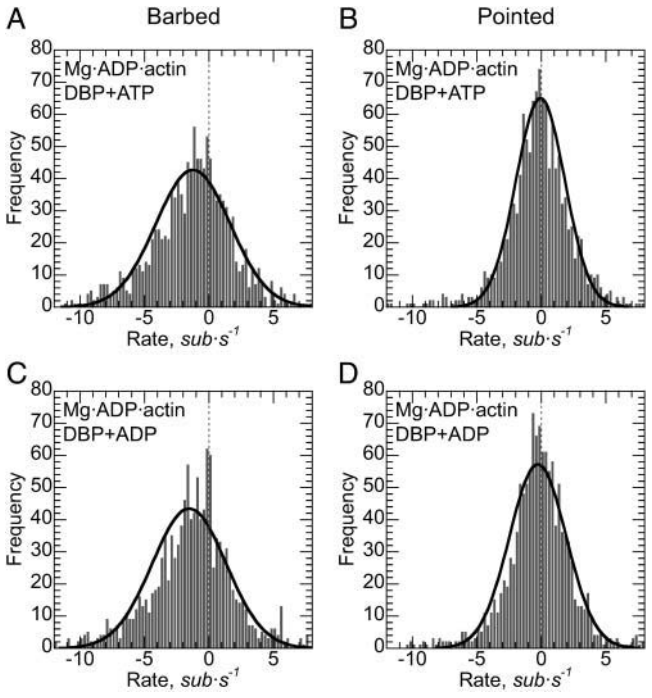


FIGURE 6 Direct measurement of subunit dissociation. Conditions: 1.5 $\mu$M Mg-ATP-actin (25% fraction label) in the same buffer as Fig. 2 was polymerized on the slide for 10 min, followed by incubation with 0.18 $\mu$M (25% label) Mg-ATP-actin for 22 min to maintain filament length during phosphate release and followed by 1.5 $\mu$M (50% label) Mg-ATP-actin for 1–2 min to mark barbed ends. Filaments were depolymerized in either ATP or ADP buffer with 5 $\mu$M vitamin D binding protein to sequester free actin monomers. Barbed ends of marked filaments depolymerized faster than pointed ends. Unmarked filament ends were categorized as barbed or pointed based on their average depolymerization rate. Smoothed instantaneous growth rates (see Fig. 2) of marked and unmarked filaments were combined, binned into 0.5 $s^{-1}$ increments, and plotted as a histogram (*shaded bars*) of observation frequency for the (*A* and *C*) barbed and (*B* and *D*) pointed end. Gaussian distributions (*solid lines*) of equivalent mean and standard deviation are shown for comparison. (*A* and *B*) Depolymerization of Mg-ADP-actin filament (*A*) barbed ends and (*B*) pointed ends in ATP buffer. Barbed ends depolymerized at 1.23 $\pm$ 2.88 $s^{-1}$ (mean $\pm$ SD) and pointed ends at 0.06 $\pm$ 1.89 $s^{-1}$. (*C* and *D*) Depolymerization of Mg-ADP-actin filament (*C*) barbed ends and (*D*) pointed ends in ADP buffer. Rates were 1.52 $\pm$ SD of 2.86 $s^{-1}$ at the barbed end and 0.26 $\pm$ 2.20 $s^{-1}$ at the pointed end.

elongated at $0.839 \pm 0.013$ $s^{-1}$ ($N = 10$ filaments), faster than the average rate of shortening of pointed ends, $0.125 \pm 0.012$ $s^{-1}$ ($N = 10$ filaments). ''Straightened'' kymographs of these filaments (Fig. 7 *B*) show that barbed ends elongated at a constant rate, whereas pointed ends shortened intermittently. Uncertainty in the measurements of length changes at pointed ends precluded a detailed analysis of these pauses.

To avoid potential effects of marked ends on treadmilling, we used filaments uniformly labeled with a single mol fraction OG-actin and myosin attachment points as fiducial marks. Uniformly labeled filaments treadmilled like end-labeled filaments (not shown). At low concentrations of Mg-ATP-actin monomers, barbed end elongation rates depended on the mol fraction of unlabeled actin monomers, as at high concentrations. The effect of labeled subunits on elongation at the pointed ends was ambiguous due to the scatter of the depolymerization rates.

Assigning ends from polymerization rates is ambiguous at low actin concentrations. Although barbed ends grow faster at all concentrations above the critical concentration, they also shorten faster than pointed ends below some ''crossover'' concentration owing to a higher dissociation rate constant. To determine the crossover concentration, we swapped barbed and pointed end assignments for concentrations at or below some arbitrary concentration and reanalyzed the rate as a function of concentration data for both ends. The best linear fits, measured from the sum of the correlation coefficients ($R^2$ values) at both ends, were achieved with a crossover concentration of 50 nM unlabeled actin ($R_b^2 = 0.91$, $R_p^2 = 0.53$). Below this concentration barbed ends depolymerized faster.

Plots of elongation rate versus concentration of unlabeled Mg-ATP-actin at these low actin concentrations (Fig. 8, *A* and *B*) gave the following rate constants: barbed end association rate constant $k_+^b = 13.9 \pm 1.7\,\mu M^{-1}\,s^{-1}$; barbed end dissociation rate constant $k_-^b = 0.89 \pm 0.15\,s^{-1}$; pointed end association rate constant $k_+^p = 0.7 \pm 0.5\,\mu M^{-1}\,s^{-1}$; and pointed end dissociation rate $k_-^p = 0.19 \pm 0.04\,s^{-1}$. We did not observe balanced barbed end polymerization and pointed end depolymerization at any concentration, thus filaments never reached a steady state with the monomer pool during our observation window. Although barbed ends switched from depolymerization to elongation at higher concentrations, pointed ends did not elongate under these conditions.

## Global analysis of combined elongation data

We combined our elongation data for all actin concentrations to arrive at a global fit of rate as a function the concentration of unlabeled actin monomers (Fig. 8, *C* and *D*). The barbed end association rate constant was $k_+^b = 7.4 \pm 0.5\,\mu M^{-1}\,s^{-1}$ and the dissociation rate constant was $k_-^b = 0.8 \pm 0.8\,s^{-1}$. The pointed end association rate constant was $k_+^p = 0.56 \pm 0.10\,\mu M^{-1}\,s^{-1}$ and the dissociation rate constant was $k_-^p = 0.44 \pm 0.17\,s^{-1}$. The linear fit to the barbed end data ($R^2 = 0.83$) was more robust than the pointed end data ($R^2 = 0.39$). Table 1 compares our TIRF microscopy measurements with rate constants measured by electron microscopy.

## DISCUSSION

To observe polymerization and depolymerization of single actin filaments over a wider range of actin monomer concentrations, we improved the total internal reflection fluorescence microscopy method (Amann and Pollard, 2001; Fujiwara et al., 2002). This required a new actin labeling

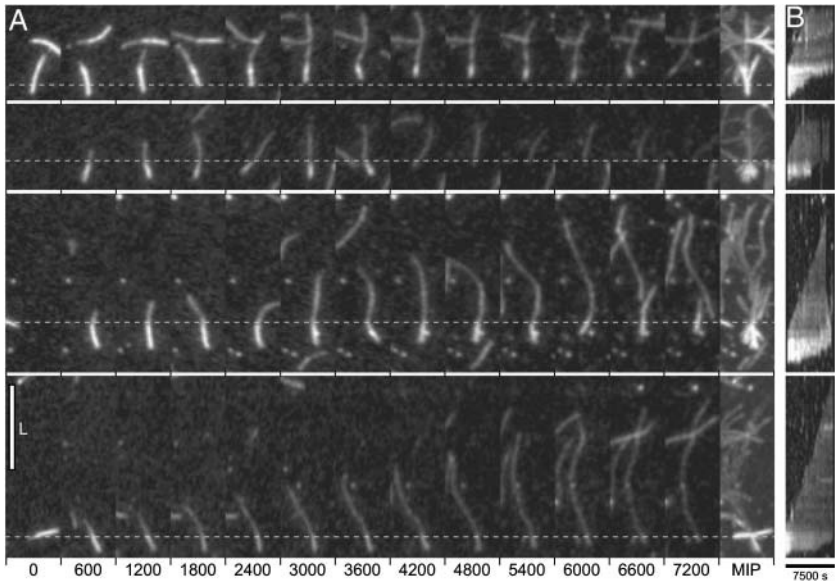


FIGURE 7 Treadmilling of subunits through actin filaments at low concentrations of monomers. Conditions: Mg-ATP-actin in same buffer as Fig. 2. Labeled ends were created by growing filaments with sequential washes of 5 $\mu$M 50% labeled actin, followed by 5 $\mu$M, 35% labeled actin and observed in the presence of 0.15 $\mu$M, 25% labeled actin. (*A*) Life histories of four filaments are shown as a sequence of images, with time given in seconds in the horizontal direction. (*MIP*) The right panel shows a maximum intensity projection of the sequence. Dashed lines show the position of a stationary fiducial mark for each filament. Filaments are oriented with shrinking pointed ends (bright fluorescence) to the bottom and growing barbed ends to the top. Length scale bar (*L*) at left is 10 $\mu$m. (*B*) Each filament is presented as a ''straightened'' kymograph, where filament intensity was sampled at equally spaced intervals along its length (vertical direction) for each frame in the sequence (horizontal direction, time increasing toward bottom). Vertical dimensions are the same as the scale bar in panel *A*. Total width of kymograph represents 7500 s.

scheme, autofocusing, drift correction, and improvements in filament length measurement.

Actin labeled on Cys-374 with Oregon green 488 iodoacetamide is brighter than rhodamine labeled actin used in earlier TIRF studies. Like rhodamine actin, OG-actin incorporated into actin filaments but did not contribute to the elongation rate. We extrapolated the rate constants measured at several mol fractions of labeled actin to obtain the rate constants for native actin polymerization, which depended solely on the concentration of unlabeled actin in the reaction.

Each filament needs a stable fiducial mark to distinguish growth at the two ends. For this purpose Fujiwara et al. (2002) used bright fiducial spots on rare actin filaments to demonstrate steady-state treadmilling. We used two methods to distinguish barbed and pointed ends of numerous filaments. In some experiments we pulse-labeled filaments with different fractions of labeled actin to mark a stable boundary. For uniformly labeled filaments, we located points where NEM-inactivated myosin attached filaments to the glass surface as stable external fiducial marks. Residual analysis of growth curves distinguished these myosin attachment points from nonspecific binding of filaments to glass. Although subtle, the intensity variations along each filament revealed by kymographs (Fig. 2 *B*) are internal fiducial marks that are potentially superior to external marks.

We used these methods to obtain simultaneously the rate constants for both filament ends in each experiment, allowing measurement of hundreds of filaments. At all actin monomer concentrations occasional pauses separated periods of constant growth or shrinkage. Although pauses were more frequent at barbed ends, pauses also occurred during long-term pointed end depolymerization under filament treadmilling conditions. Measurement noise likely obscured many pointed end pauses, owing to very slow changes in length relative to measurement errors.

What accounts for these pauses? Contaminating capping protein (McLean-Fletcher and Pollard, 1980) might cause barbed end pauses, but the 38-s average half-life of barbed end pauses (not shown) is far shorter than the 4500-s half-time for capping protein dissociation (Schafer et al., 1996). Furthermore, reducing capping protein contamination by double gel filtration of actin did not reduce the frequency or duration of pauses. Association with inactive myosin might cause pauses. Many growing filaments paused when an end affixed to a single point, consistent with myosin binding. Some filaments shortening at low actin concentrations also paused at a presumptive NEM-myosin attachment point. Since we and others (Fujiwara et al., 2002) observed pauses in the absence of myosin, pauses are more likely due to nonspecific, unfavorable interactions of filament ends with the glass surface. Consistent with this interpretation, growth pauses and filament attachment (seen as decreased Brownian motion) are more common in winter, when lower humidity can increase electrostatic charges on the glass surfaces.

Real-time fluorescence microscopy confirmed that the rate constant for elongation of barbed ends by Mg-ATP-actin of $7.4 \pm 0.5\ \mu M^{-1}\ s^{-1}$ is ~10 times larger than the pointed end association rate constant of $0.56 \pm 0.10\ \mu M^{-1}\ s^{-1}$. These values fall within the range of previous measurement, for example 3.4–12.3 $\mu M^{-1}\ s^{-1}$ at the barbed end (see Pollard, 1986; Table 2). Both TIRF microscopy values are ~65% the values measured by electron microscopy. Undetectable pauses could partially account for the lower rates measured by TIRF microscopy, but EM measurements could have overestimated growth rates. For electron microscopy, filaments were grown from blunt-ended fragments of *Limulus* acrosomal processes and bundled with poly-L-lysine. The maximum length of the tapered bundle was measured at each time point. Given the distribution of filament growth rates we observed in individual TIRF experiments (see Fig. 5, *A* and

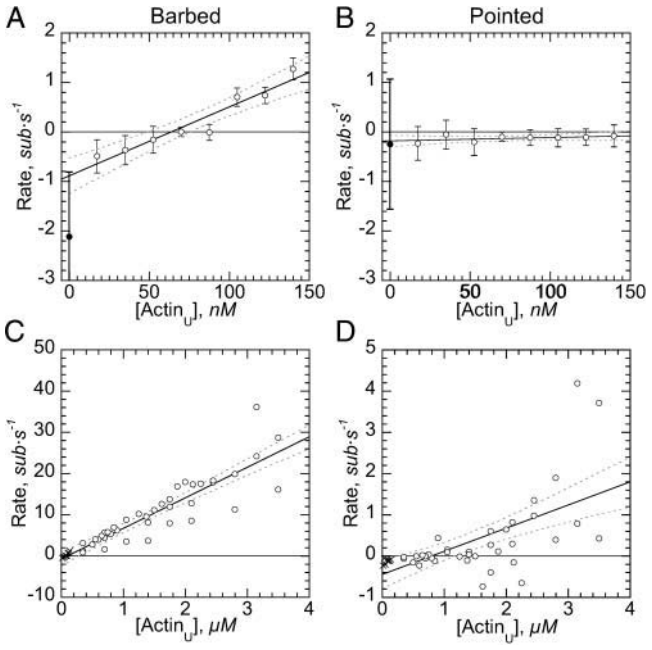


FIGURE 8 Dependence of elongation rates on actin concentration. (*A* and *B*) Behavior of (*A*) barbed ends and (*B*) pointed ends at low concentrations of Mg-ATP-actin. Conditions: 5 $\mu$M Mg-ATP-actin with 30% fraction label in the same polymerization buffer as Fig. 2. A single fraction label was used in each experiment. After polymerization of seeds, the chamber was washed with polymerization buffer containing from 0.025 to 0.2 $\mu$M total actin monomer with the same fraction labeled. The plots show rates as a function of the concentration of unlabeled actin for (○) all the low actin concentrations tested. Rate constants of $k_+^B = 13.9 \pm 1.7\,s^{-1} \cdot \mu M^{-1}$, $k_-^B = 0.89 \pm 0.15\,s^{-1}$, $k_+^P = 0.7 \pm 0.5\,s^{-1} \cdot \mu M^{-1}$, $k_-^P = 0.19 \pm 0.04\,s^{-1}$ were obtained by linear regression. Mg-ATP-actin depolymerization rates (●) are shown for comparison. (*C* and *D*) Global summary of the polymerization rates at (*C*) barbed ends and (*D*) pointed ends as a function of unlabeled actin concentration for low (×) and high (○) actin concentrations. Rate constants of $k_+^B = 7.4 \pm 0.5\,s^{-1} \cdot \mu M^{-1}$, $k_-^B = 0.8 \pm 0.8\,s^{-1}$, $k_+^P = 0.56 \pm 0.10\,s^{-1} \cdot \mu M^{-1}$, $k_-^P = 0.44 \pm 0.17\,s^{-1}$ were obtained by linear regression. The linear regression is the solid line and the upper and lower 95% confidence intervals are dashed lines.

*B*), it is likely that measuring the longest filament in EM overestimated growth rates. Fitting our rate constants to the fastest filament in each experiment (Fig. 8, *C* and *D*, *circles*) gave rate constants ($k_+^b$ of 10.7 $\mu M \cdot s^{-1}$ and $k_+^p$ of 1.5 $\mu M \cdot s^{-1}$) similar to the EM method.

Polymerization rate constants measured by fluorescence microscopy varied from experiment to experiment (Fig. 5). Environmental conditions such as humidity, temperature, and charge on the glass substrate are more likely to explain the variation in our measurements than differences in actin activity, because we obtained trials 2 and 3 on successive days using the same actin preparation. Thus, internal controls are essential when using microscopy to study the effects of solution conditions or regulatory proteins on actin polymerization rates. As TIRF microscopy becomes a standard method for actin kinetics, polymerization rates of actin alone should be routinely remeasured for each set of experimental conditions.

## Methods to measure dissociation rate constants

Previous estimates of subunit dissociation rates relied on bulk samples with unknown numbers of filament ends (Carlier et al., 1986; Teubner and Wegner, 1998) or on microscopic measurements of elongation rates at actin monomer concentrations above the critical concentration and linear extrapolation of these rates to zero monomer (Pollard, 1986). We observed subunit dissociation directly in excess vitamin D binding protein to sequester monomers and preclude association reactions. This allowed us to test the effects of nucleotides on subunit dissociation.

Dissociation rate constants obtained by extrapolation of linear plots of growth rates versus actin monomer concentrations to zero monomer concentration are inherently more sensitive to measurement noise than those obtained by direct measurement. Our association rate constants varied 2.5-fold between different trials, whereas our dissociation rate constants obtained by extrapolation varied 10-fold between trials. Over seven trials of Mg-ATP-actin growth by EM, Pollard (1986) observed a 1.3-fold range of barbed-end association rate constants and a 10-fold range of extrapolated barbed-end dissociation rate constants.

## Depolymerization at barbed ends

We created Mg-ADP-actin filaments by incubating filaments assembled from Mg-ATP-actin monomers for 22 min in a concentration of ATP-actin monomers where pointed ends depolymerized and barbed-end polymerization was slow and stochastic, growing at most 500 subunits (not shown). During this ageing step most subunits in the filaments hydrolyzed their bound ATP (1000 half-lives) and dissociated the $\gamma$-phosphate (five half-lives) to become ADP-actin. Short barbed end caps that grew during ageing consisted of a mixture of Mg-ATP- Mg-ADP-Pi- and Mg-ADP-actin. Some of these short caps broke off when the actin monomers were washed out; the rest depolymerized within 300 s.

We did not confirm that the ATP in the buffer slows dissociation of Mg-ADP-actin subunits at the barbed end as reported by Teubner and Wegner (1998). When vitamin D binding protein sequestered free subunits, Mg-ADP-actin dissociated from barbed ends at 1.2 $s^{-1}$ in ATP buffer and 1.5 $s^{-1}$ in ADP buffer. A two-tailed student's *t*-test showed little significant difference between these two conditions (*p*-value of 0.071).

## Inferred dissociation rate constants at barbed ends

To evaluate the dissociation rate constants for Mg-ATP-actin, we observed changes in the length of filaments at Mg-ATP-actin monomer concentrations near or below the critical concentration. Under these conditions, Mg-ATP-actin associates with barbed ends at a rate proportional to its concentration. Because the half times are ~2 s for hydrolysis

**TABLE 1 Summary of rate constants**

| Experiment | Barbed end | | | Pointed end | | | Number | | |
|---|---|---|---|---|---|---|---|---|---|
| | $k_+$ | $k_-$ | $K_d$ | $k_+$ | $k_-$ | $K_d$ | Reactions | Filaments | Points |
| | $\mu M^{-1}\cdot s^{-1}$ | $s^{-1}$ | $\mu M$ | $\mu M^{-1}\cdot s^{-1}$ | $s^{-1}$ | $\mu M$ | | | |
| 0.5–5 $\mu$M Mg-ATP-actin | 7.5 ± 0.7 | 1.0 ± 1.2 | 0.13 ± 0.17 | 0.66 ± 0.14 | 0.7 ± 0.2 | 1.06 ± 0.53 | 39 | 412 | 15,664 |
| 0.025–0.2 $\mu$M Mg-ATP-actin | 13.9 ± 1.7 | 0.89 ± 0.15 | 0.06 ± 0.02 | 0.7 ± 0.5 | 0.19 ± 0.04 | 0.3 ± 0.3 | 8 | 69 | 1193 |
| Combined | 7.4 ± 0.5 | 0.8 ± 0.8 | 0.11 ± 0.12 | 0.56 ± 0.10 | 0.44 ± 0.17 | 0.8 ± 0.4 | | | |
| Mg-ADP-actin depolymerized in ATP | – | 1.23 ± 2.88 | – | – | 0.06 ± 1.89 | – | 3 | 38 | 1233 |
| Mg-ADP-actin depolymerized in ADP | – | 1.52 ± 2.86 | – | – | 0.26 ± 2.20 | – | 3 | 37 | 1246 |
| Combined | – | 1.37 ± 2.87 | – | – | 0.16 ± 2.05 | – | | | |
| Mg-ATP-actin (Pollard, 1986) | 11.6 | 1.4 | 0.12 | 1.3 | 0.8 | 0.62 | – | – | – |
| Mg-ADP-actin (Pollard, 1986) | 3.8 | 7.2 | 1.89 | 0.16 | 0.27 | 1.69 | – | – | – |

(Blanchoin and Pollard, 2002) and 5 min for phosphate dissociation (Melki et al., 1996), most terminal subunits will have bound ATP or ADP-Pi (Bindschadler et al., 2004). Linear extrapolation of the rate of elongation (including negative values below the critical concentration) of plots of rate versus actin concentration to zero actin gave a dissociation rate constant of 0.9 $s^{-1}$ for these species on the end of the filament. This is two-thirds the average rate of ADP-actin dissociation we observed in the presence of DBP to sequester monomers. Thus, even rare associations of ATP monomers protect barbed ends from the higher rate of ADP-actin dissociation.

Previous estimates of Mg-ATP-actin barbed end dissociation rate constants based on extrapolation of polymerization conditions showed similar rate constants of 1.4 $s^{-1}$ (Pollard, 1986) or 0.14–4.6 $s^{-1}$ (Carlier et al., 1986). Our direct measurement of Mg-ADP-actin dissociation from barbed ends was only 1.5-fold higher than the ''ATP-actin'' dissociation rate, rather than the three- to fourfold higher values for Mg-ADP-actin than Mg-ATP-actin dissociation reported previously (7.2 $s^{-1}$, Pollard, 1986; 6.0 $s^{-1}$, Carlier et al., 1986; or 11.5 $s^{-1}$, Teubner and Wegner, 1998).

## Depolymerization at pointed ends

Similar to the barbed end, the rates of subunit dissociation from the pointed ends were equivalent in buffer with ATP or ADP at ~0.16 $s^{-1}$. Although the mean dissociation rate of Mg-ADP-actin was greater (0.06 $s^{-1}$) in ATP buffer than ADP buffer (0.26 $s^{-1}$), a two-tailed Student's *t*-test showed that these two distributions were indistinguishable (*p*-value of 0.082). A possibility of small effect of ATP in the buffer on pointed end depolymerization is intriguing and merits further study, because the nucleotide or phosphate exchange seem more plausible at pointed ends where the nucleotide binding cleft is more exposed on the terminal subunits (Fig. 9) than at barbed ends (Holmes et al., 1990). However, events at the pointed end are likely to remain enigmatic, because the reactions are slow and the mol fraction of subunits occupying either end is miniscule compared with internal subunits (Blanchoin and Pollard, 2002).

## Inferred dissociation rate constants at pointed ends

To evaluate the dissociation rate constants for Mg-ATP-actin, we observed changes in the length of filaments at Mg-ATP-actin monomer concentrations near or below the critical concentration. Because association and dissociation reactions are very slow at pointed ends, filaments assembled from ATP-actin have more terminal subunits with bound ADP-Pi than ATP or ADP, but the mix depends on the concentrations of ADP monomers and filament ends (Bindschadler et al., 2004). Linear extrapolation of the rate of pointed end length changes with time (including negative values below the critical concentration) to zero actin gave a dissociation rate constant of 0.19 $s^{-1}$ for the mixture of species on the end of the filament, similar to the average rate of 0.16 $s^{-1}$ seen for Mg-ADP-actin. Unlike the barbed end, Mg-ATP- or Mg-ADP-Pi-monomers do not protect the pointed end from depolymerization.

## Subunit diffusion on filament ends

Our main approach was to measure rate constants directly. An alternative pioneered by Fujiwara et al. (2002) is to observe changes in the length of single actin filaments at steady state. Fujiwara et al. analyzed such changes as one-dimensional Fick's diffusion processes. They estimated a diffusion coefficient of 25 $sub^2$ $s^{-1}$ with 0.7 $\mu$M Ca-ATP-actin at steady state. From this diffusion coefficient, they estimated barbed end rate constants for Ca-ATP-actin of $k_+^D = 180\,\mu M^{-1}\,s^{-1}$ and $k_-^D = 25\,s^{-1}$ at steady state. A similar analysis with 0.3 $\mu$M Mg-ATP-actin gave a diffusion coefficient of 29 $sub^2\cdot s^{-1}$ at steady state and elongation rate constants of $k_+^D = 450\,\mu M^{-1}\,s^{-1}$ and $k_-^D = 29\,s^{-1}$. These values were 40-fold larger than those obtained from measurements of filament elongation.

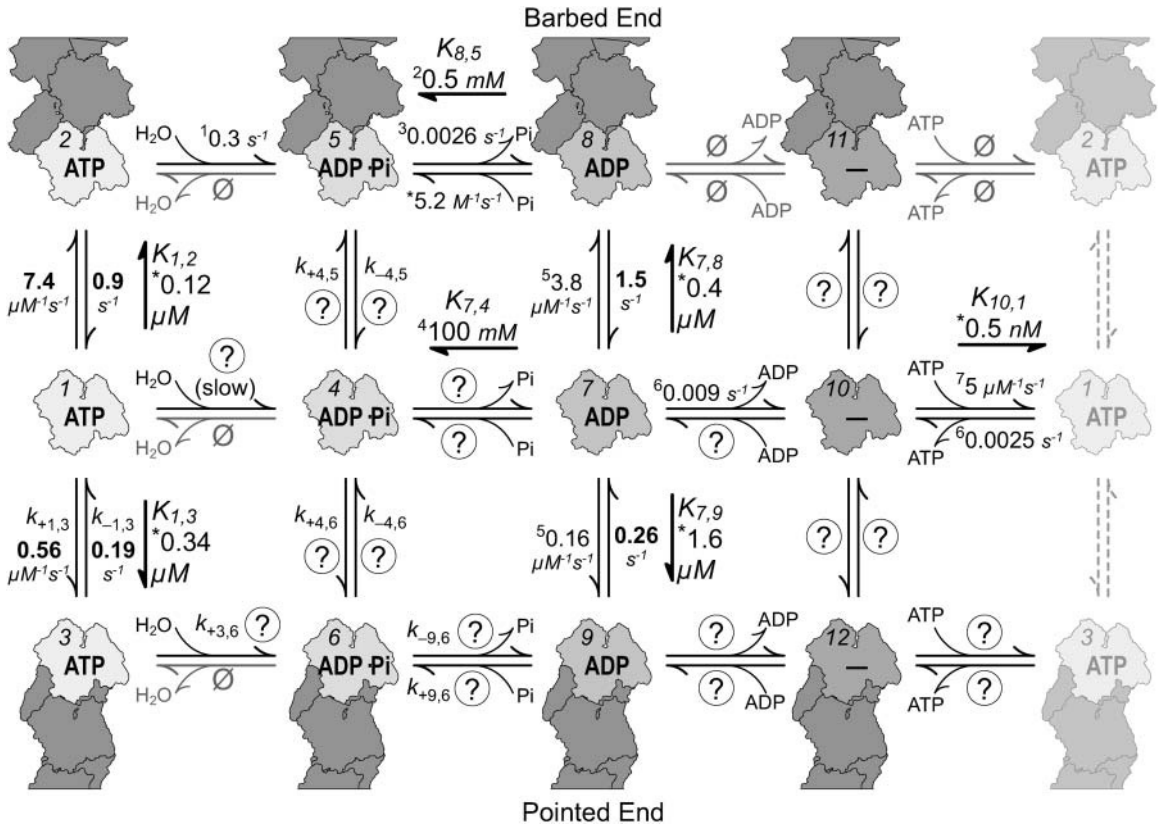


FIGURE 9 Reactions for Mg-actin polymerization and nucleotide cycling. Schematic for Mg-ATP-, Mg-ADP-Pi-, Mg-ADP-, and nucleotide free actin binding to filament barbed and pointed ends at pH 7, including nucleotide hydrolysis, phosphate release, and nucleotide exchange. Nucleotide content of internal subunits is ignored. Numbers denote rate constants measured here (*bold*) or previously (*1*, Blanchoin and Pollard, 2002; *2*, Carlier and Pantaloni, 1988; *3*, Melki et al., 1996; *4*, Wanger and Wegner, 1987; *5*, Pollard, 1986; *6*, Selden et al., 1999 ; *7*, De La Cruz and Pollard, 1995). $K_{r,p}$ indicate equilibrium constants for reactants $r$ and products $p$; $k_{+r,p}$, association rate; $k_{-r,p}$, dissociation rate; ?, unknown rate constants; Ø, highly unfavorable reactions; *, calculated rate or equilibrium constants.

We, too, observed changes in length of actin filaments at Mg-ATP-actin monomer concentrations near the steady-state critical concentration. We confirmed that single filaments can treadmill, growing at their barbed ends and shrinking at their pointed ends. Although our filaments never reached steady state, we performed the diffusion analysis of Fujiwara et al. (2002) for the actin concentration closest to steady state treadmilling (0.15 $\mu$M) and obtained a diffusion constant of 31 sub$^2\cdot$s$^{-1}$ and diffusion-based rate constants $k_+^D = 230\,\mu M^{-1}\,s^{-1}$ and $k_-^D = 31\,s^{-1}$ (not shown). In our experiment, barbed ends grew at an average rate of 0.8 $s^{-1}$, whereas pointed ends shortened at an average rate of 0.13 $s^{-1}$, far from the 40-fold difference in rate constants of Fujiwara et al.

To account for the differences between rate constants measured directly and by diffusion, Fujiwara et al. (2002) proposed that the unit of polymerization is, on average, five to six subunits rather than one. We observed several filament annealing events at high actin concentrations, but large-scale annealing events were far more frequent at low actin concentrations where we observed filaments over longer time courses. Although we removed obvious annealing events from our analysis, undetectable annealing of short segments is conceivable.

Any phenomena that increases the deviation between individual filament growth rates over time creates an apparent diffusion constant larger that one subunit. The stochastic pauses in filament growth described above are one such phenomenon. Although we removed most of the obvious filament pauses from our analysis of linear growth, pauses either shorter than the frame period of 8–30 s or hidden by measurement error would have increased the dispersion in growth rates between individual filaments and effectively decreased the apparent association rate constants. Our measured association rate constants were lower at both ends than those measured by EM (Pollard, 1986), supporting the idea that undetectable pauses contributed to filament growth and thus to the large diffusion constant.

Measurement error that increases with time can also contribute to large apparent diffusion constants. We and others (Fujiwara et al., 2002) estimate filament length by piecewise linear approximation, but filament bending can

lead to considerable measurement error. Changes in length measured over short periods have small errors, owing to the similar filament curvature, whereas slow changes in curvature introduce considerably more error into length changes measured over longer time spans. The persistence length of actin filaments is 10 $\mu$m (Isambert et al., 1995; Liu and Pollack, 2002; Yanagida et al., 1984), meaning that filaments can bend 10° in as little as 1.2 $\mu$m. We observed Brownian bending along the entire length of growing actin filaments, and as filaments treadmilled through subunits, their curvature evolved slowly (Fig. 2 *A*). Kymographs of filaments ''straightened'' by piecewise linear approximation (Figs. 2 *B* and 7 *B*) show that stable fiducial marks along a filament fail to align at later time points, illustrating the increase in measurement error from slow changes in filament curvature.

Annealing, pauses, and bending contribute to larger deviation in growth rates as filaments elongate. A more detailed TIRF microscopy study of filament annealing and pauses, along with improved spline-based estimates of filament length should clear up this ambiguity between estimated diffusion and observed rate constants.

### Steady-state behavior

The behavior of the ends of actin filaments at steady state in the presence of ATP and actin monomers is very complicated owing to a large number of interconnected reactions (Fig. 9). Mathematical models of filament behavior depend on accurate measurements of subunit association and dissociation, ATP binding to monomers, ATP hydrolysis by actin polymerized subunits, dissociation and reassociation of the $\gamma$-phosphate on monomeric and polymerized ADP-actin subunits, and dissociation of ADP from actin monomers (Bindschadler et al., 2004). Some of the assumptions and reaction rates required to complete the analysis of this complex system are still lacking (Fig. 9, *question marks*), whereas other rates gathered from the literature may bear further scrutiny.

One unresolved issue is the affinity of ADP-actin monomers for phosphate. Wanger and Wegner (1987) used polymerization assays to estimate the affinities of phosphate for ADP-actin filaments ($K_d$ = 10 mM; i.e., $K_{8,5}$) and monomers ($K_d$ = 100 mM; i.e., $K_{7,4}$). However, they did not determine which ionic species of Pi participates, nor did they correct for the contributions of sodium-phosphate to the ionic strength. Carlier and Pantaloni (1988) did balance the ionic strength and identified $H_2PO_4^-$ as the only species that binds ADP-actin filaments. The affinity of $H_2PO_4^-$ for ADP-actin filaments is 0.5 mM (i.e., $K_{8,5}$), 20-fold stronger than the 10 mM measured by Wanger and Wegner (1987). Since in Wanger and Wegner's calculation the affinity of phosphate for monomers depended on its affinity for filaments, the affinity of $H_2PO_4^-$ for ADP-actin monomer may also be 20 times higher (i.e., $K_{7,4}$ = 5 mM). An important goal for the field is to fill in these missing experimental parameters.

We profusely thank our anonymous reviewers for their many valuable observations and comments. We also thank Ernesto Andrianantoandro for help in developing the actin labeling protocol and other members of the Pollard lab for technical assistance and helpful discussions.

This work was supported by National Institutes of Health research grant GM-26338 (to T. D. Pollard) and a Burroughs Wellcome Fund Career Award at the Scientific Interface (to J. R. Kuhn).

## REFERENCES

Amann, K. J., and T. D. Pollard. 2001. Direct real-time observation of actin filament branching mediated by Arp2/3 complex using total internal reflection microscopy. *Proc. Natl. Acad. Sci. USA*. 98:15009–15013.

Bindschadler, M., E. A. Osborn, C. F. Dewey, Jr., and J. L. McGrath. 2004. A mechanistic model of the actin cycle. *Biophys. J*. 86:2720–2739.

Blanchoin, L., K. J. Amann, H. N. Higgs, J. B. Marchand, D. A. Kaiser, and T. D. Pollard. 2000. Direct observation of dendritic actin filament networks nucleated by Arp2/3 complex and WASp/Scar proteins. *Nature*. 404:1007–1011.

Blanchoin, L., and T. D. Pollard. 2002. Hydrolysis of bound ATP by polymerized actin depends on the bound divalent cation but not profilin. *Biochemistry*. 41:597–602.

Bonder, E. M., and M. S. Mooseker. 1986. Cytochalasin B slows but does not prevent monomer addition at the barbed end of the actin filament. *J. Cell Biol*. 102:282–288.

Burlacu, S., P. A. Janmey, and J. Borejdo. 1992. Distribution of actin filament lengths measured by fluorescence microscopy. *Am. J. Physiol*. 262:C569–C577.

Carlier, M.-F., P. Criquet, D. Pantaloni, and E. D. Korn. 1986. Interaction of cytochalasin-D with actin filaments in the presence of ADP and ATP. *J. Biol. Chem*. 261:2041–2050.

Carlier, M. F., V. Laurent, J. Santolini, R. Melki, D. Didry, G. X. Xia, Y. Hong, N. H. Chua, and D. Pantaloni. 1997. Actin depolymerizing factor (ADF/cofilin) enhances the rate of filament turnover: implication in actin-based motility. *J. Cell Biol*. 136:1307–1322.

Carlier, M.-F., and D. Pantaloni. 1988. Binding of phosphate to F-ADP-actin and role of F-ADP-Pi-actin in ATP-actin polymerization. *J. Biol. Chem*. 263:817–825.

Cintio, O., R. Adami, D. Choquet, and E. Grazi. 2001. On the elastic properties of tetramethylrhodamine F-actin. *Biophys. Chem*. 92:201–207.

De La Cruz, E., and T. D. Pollard. 1995. Nucleotide-free actin: stabilization by sucrose and nucleotide binding kinetics. *Biochemistry*. 34:5452–5461.

Detmers, P., A. Weber, M. Elzinga, and R. E. Stephens. 1981. 7-Chloro-4-nitrobenzo-2-oka-1, 3-diazole actin as a probe for actin polymerization. *J. Biol. Chem*. 256:99–105.

Fujiwara, I., S. Takahashi, H. Tadakuma, T. Funatsu, and S. Ishiwata. 2002. Microscopic analysis of polymerization dynamics with individual actin filaments. *Nat. Cell Biol*. 4:666–673.

Holmes, K. C., D. Popp, W. Gebhard, and W. Kabsch. 1990. Atomic model of the actin filament. *Nature*. 347:44–49.

Houk, T. W., Jr., and K. Ue. 1974. The measurement of actin concentration in solution: a comparison of methods. *Anal. Biochem*. 62:66–74.

Huxley, H. E., and W. Brown. 1967. The low-angle x-ray diagram of vertebrate striated muscle and its behavior during contraction and rigor. *J. Mol. Biol*. 30:383–434.

Ichetovkin, I., W. Grant, and J. Condeelis. 2002. Cofilin produces newly polymerized actin filaments that are preferred for dendritic nucleation by the Arp2/3 complex. *Curr. Biol*. 12:79–84.

Isambert, H., P. Venier, A. C. Maggs, A. Fattoum, R. Kassab, D. Pantaloni, and M. F. Carlier. 1995. Flexibility of actin filaments derived from

thermal fluctuations. Effect of bound nucleotide, phalloidin, and muscle regulatory proteins. *J. Biol. Chem.* 270:11437–11444.

Jähne, B. 2002. Digital Image Processing. Springer-Verlag, Berlin, Germany.

Kielley, W. W., and W. F. Harrington. 1959. A model for the myosin molecule. *Biochim. Biophys. Acta.* 41:401–421.

Kouyama, T., and K. Mihashi. 1981. Fluorimetry study of N-(1-pyrenyl)-iodoacetamide labelled F-actin. *Eur. J. Biochem.* 114:33–38.

Kovar, D. R., J. R. Kuhn, A. L. Tichy, and T. D. Pollard. 2003. The fission yeast cytokinesis formin Cdc12p is a barbed end actin filament capping protein gated by profilin. *J. Cell Biol.* 161:875–887.

Kron, S. J., and J. A. Spudich. 1986. Fluorescent actin filaments move on myosin fixed to a glass surface. *Proc. Natl. Acad. Sci. USA.* 83:6272–6276.

Liu, X., and G. H. Pollack. 2002. Mechanics of F-actin characterized with microfabricated cantilevers. *Biophys. J.* 83:2705–2715.

McLean-Fletcher, S., and T. D. Pollard. 1980. Identification of a factor in conventional muscle actin preparations which inhibits actin filament self association. *Biochem. Biophys. Res. Commun.* 96:18–27.

McLeod, J. F., M. A. Kowalski, and J. G. Haddad, Jr. 1989. Interactions among serum vitamin D binding protein, monomeric actin, profilin, and profilactin. *J. Biol. Chem.* 264:1260–1267.

Melki, R., S. Fievez, and M.-F. Carlier. 1996. Continuous monitoring of Pi release following nucleotide hydrolysis in actin or tubulin assembly using 2-amino-6-mercapto-7-methylpurine ribonucleoside and purine-nucleoside phosphorylase as an enzyme-linked assay. *Biochemistry.* 35:12038–12045.

Oosawa, F., and S. Asakura. 1975. Thermodynamics of the Polymerization of Protein. Academic Press, New York.

Pollard, T. D. 1986. Rate constants for the reactions of ATP- and ADP-actin with the ends of actin filaments. *J. Cell Biol.* 103:2747–2754.

Pollard, T. D., and M. S. Mooseker. 1981. Direct measurement of actin polymerization rate constants by electron microscopy of actin filaments nucleated by isolated microvillus cores. *J. Cell Biol.* 88:654–659.

Schafer, D. A., P. B. Jennings, and J. A. Cooper. 1996. Dynamics of capping protein and actin assembly in vitro: uncapping barbed ends by polyphosphoinositides. *J. Cell Biol.* 135:169–179.

Selden, L. A., H. J. Kinosian, J. E. Estes, and L. C. Gershman. 1999. Impact of profilin on actin-bound nucleotide exchange and actin polymerization dynamics. *Biochemistry.* 38:2769–2778.

Spudich, J. A., and S. Watt. 1971. The regulation of rabbit skeletal muscle contraction. I. Biochemical studies of the interaction of the tropomyosin-troponin complex with actin and the proteolytic fragments of myosin. *J. Biol. Chem.* 246:4866–4871.

Teubner, A., and A. Wegner. 1998. Kinetic evidence for a readily exchangeable nucleotide at the terminal subunit of the barbed ends of actin filaments. *Biochemistry.* 37:7532–7538.

Wanger, W., and A. Wegner. 1987. Binding of phosphate ions to actin. *Biochem. Biophys. Acta.* 914:105–113.

Wegner, A. 1976. Head to tail polymerization of actin. *J. Mol. Biol.* 108: 139–150.

Woodrum, D. T., S. A. Rich, and T. D. Pollard. 1975. Evidence for biased bidirectional polymerization of actin using heavy meromyosin prepared by an improved method. *J. Cell Biol.* 67:231–237.

Xu, J., J. F. Casella, and T. D. Pollard. 1999. Effect of capping protein, CapZ, on the length of actin filaments and mechanical properties of actin filament networks. *Cell Motil. Cytoskeleton.* 42:73–81.

Yanagida, T., M. Nakase, K. Nishiyama, and F. Oosawa. 1984. Direct observation of motion of a single actin filament in the presence of myosin. *Nature.* 307:58–60.